


Determination of two structures of the solvent 3-hydroxypropionitrile crystallized at low temperatures

Pamela S. Whitfield ^{1,2,a)} Zouina Karkar,² and Yaser Abu-Lebdeh²

¹Excelsus Structural Solutions (Swiss AG), Park Innovaare, Villigen, Switzerland

²National Research Council Canada, 1200 Montreal Road, Ottawa, Ontario, Canada K1A 0R6

(Received 1 September 2023; accepted 13 December 2023)

The title compound, 3-hydroxypropionitrile, was crystallized repeatedly *in situ* inside a quartz capillary using a liquid nitrogen cryostream. The X-ray powder diffraction patterns obtained indicated the presence of two distinct crystalline phases. The cleanest datasets for each of the phases were used to solve the crystal structures via simulated annealing, followed by refinement and optimization via dispersion-corrected density functional theory (DFT) calculations, with a final Rietveld refinement against the experimental data. The two structures appear to correspond to those proposed in a 1960s literature vibrational spectroscopy paper, one being the more stable with a *gauche* molecular conformation and the second metastable phase more complex with mixed conformations. Dispersion-corrected DFT computation using lattice parameters for both phases obtained from a single 84 K dataset with co-existing phases shows the stable and metastable phases to differ in energy by less than 0.5 kJ mol⁻¹. A comparison of experimental far infrared spectra published in the 1960s with those calculated from the proposed crystal structures provides some independent supporting evidence for the proposed structures.

© The Author(s), 2024. Published by Cambridge University Press on behalf of International Centre for Diffraction Data.

[doi:10.1017/S0885715624000010]

Keywords: structure determination, organic crystals, phase behavior, non-ambient diffraction

I. INTRODUCTION

3-hydroxypropionitrile (3-HPN; CAS 109-78-4, formula C₃H₅NO), alternatively known as 2-cyanoethanol, 3-hydroxypropanenitrile, or hydracrylonitrile, is a polar solvent with a melting point of -46 °C (227 K). In addition to use as a solvent and feedstock in organic reactions, it has also found use as a protecting agent in peptide synthesis (Misra et al., 1989), as a component in dye-sensitized solar cells (Wang et al., 2005) and as solid-state iodide-ion conductors (Wang et al., 2004, 2007). The crystal structure of the solid LiI(HPN)₂ at 293 K was determined via single-crystal X-ray diffraction (Wang et al., 2004), but no crystalline low-temperature structure of the parent 3-HPN solvent has yet appeared in the literature. Nitriles as a family have been of recent interest for possible application in lithium battery electrolytes (Abu-Lebdeh and Davidson, 2009). More recently, 3-HPN has been of interest as a possible cyano-containing molecule in interstellar space (Braakman et al., 2010). As part of a wider study of the low-temperature phase behavior of nitrile solvents, powder diffraction data were collected from crystallized 3-HPN.

Very little appears in the literature on crystalline 3-HPN, the most recent seeming to be a 1969 infrared (IR)/Raman vibrational spectroscopy paper (Schneider and Giguère, 1969) derived from a University of Laval doctoral thesis

(Schneider, 1969). Besides an amorphous glassy form, they reported the existence of two crystalline forms, one more readily obtained than the other. Early papers on 3-HPN considered the relative stabilities of *gauche* and *trans* isomers as singular entities, the *gauche* conformation being confirmed as preferred but not exclusive in the liquid state (Schneider and Giguère, 1969). The more readily obtained crystalline form (crystal-II) was assigned as containing only the *gauche* conformation, while the “metastable” form (crystal-I) contained at least a fraction of the *trans* conformation (Schneider, 1969). For some unexplained reason, Schneider and Giguère (1969) neglected the possibility of a second *gauche* conformation in 3-HPN that was mentioned by the same research group in a parallel paper on 2-chloro and 2-bromo-ethanol (Buckley et al., 1969). Another complicating factor is that Schneider (1969) and Schneider and Giguère (1969) used diametrically opposing conventions when assigning the terms crystal-I and crystal-II. This work uses the convention of Buckley and Giguère (1967) also used for Schneider and Giguère (1969) with crystal-II the more readily obtained crystalline form of 3-HPN.

At first glance, the preference for *gauche* conformation in 3-HPN appears to go against the trend of an energetic preference for *trans* isomers in such molecules due to a reduction in repulsive steric interactions. However, the nitrile group can act as a proton acceptor (Schleyer et al., 1958; Krueger and Mettee, 1965), producing significant stabilizing intramolecular hydrogen bonding in the *gauche* conformation that is not available to *trans* isomers. The crystal structure of the closely

^{a)} Author to whom correspondence should be addressed. Electronic mail: whitfieldps1@gmail.com



related molecule succinonitrile (hydroxyl group replaced by another nitrile group) also prefers the *gauche* conformation but is dominated by relatively strong intermolecular C–H...N hydrogen bonds (Whitfield et al., 2008). Later computational studies on isolated molecules quantified the difference in energies, as well as modifications to the usual *gauche* and *trans* conformations caused by the motion of the hydroxyl hydrogen atom (Roux et al., 2007). As alluded to previously, these modified *gauche* and *trans* conformations were not considered by Schneider and Giguère (1969) when assigning the IR spectral bands from solid, crystallized 3-HPN.

Studying the crystalline phase of samples that are in the liquid state at room temperature poses a challenge with the preparation of suitable samples. Special preparation and handling procedures are usually required for such single-crystal or powder diffraction studies, probably a contributing factor to gaps in the literature for even quite simple systems. Samples suitable for structure solution from powder diffraction data require good particle statistics so rapid crystallization to maintain small crystallite size is desirable. Conversely, single-crystal specimens benefit from the time to grow larger crystals with slow cooling.

Some neutron powder diffraction studies of such systems have crystallized the sample *ex situ* in bulk prior to cold grinding in a mortar and pestle prior to “cold-loading” into the sample can (e.g. David and Ibberson, 1992; Ibberson et al., 1995). This approach has obvious safety and practical issues where potentially hurried sample handling and transfer at cryogenic temperatures is required. An alternative approach is to crystallize the sample *in situ* within the sample holder, be it in a capillary for X-ray diffraction (Whitfield et al., 2008) or vanadium sample can for neutron diffraction studies (Whitfield, 2023). The *in situ* crystallization route risks the formation of large crystallites or a sample that remains amorphous. Multiple attempts are often required to determine the optimal crystallization conditions and reproducibility. Keeping the crystallite size under control is the driver for striving for as fast crystallization as achievable. An effective approach for many samples has been to form a glass via quenching the sample to cryogenic temperatures prior to rapid heating of the sample to near melting. In many cases, the resulting temperature gradient along the capillary triggers very rapid crystallization on heating when approaching the melting point. Temperature gradients have long been used to promote the crystallization of glasses (Grauer and Hamilton, 1950), and the method is analogous in some regards to the zone-melting and Bridgman approaches for producing single crystals of otherwise liquid or volatile compounds (Abrahams et al., 1950; Brodalla et al., 1985). The addition of an inert material solid dispersed in the liquid sample additionally provides copious nucleating sites to encourage simultaneous crystallization at many sites. Such rapid crystallization is desirable to avoid the formation of large crystallites, but these capillary samples are frequently associated with significant and sometimes severe preferred orientation (Whitfield et al., 2008). The temperature gradient along the sample capillary that promotes crystallization also encourages directional crystal growth. Significant texture in a powder diffraction sample used to be an absolute contraindication to a structure solution from the dataset. Such texture is to be expected in this system. Schneider (1969) described the crystallized samples for IR analysis as “1 mm long rods” and “flowers of fine needles” for the crystal-II and crystal-I

phases, respectively. However, recent developments where preferred orientation can be applied in a stable manner during extended simulated annealing runs (Whitfield et al., 2008; Whitfield, 2009) have eased this somewhat, but the additional parameters that this approach requires hinder the search for the global minimum.

II. EXPERIMENTAL

Commercial 3-hydroxypropionitrile (Aldrich 99%) was injected using a syringe into a 1 mm diameter quartz capillary. Ground quartz glass was added to the capillary prior to injecting the liquid to provide adequate nucleating sites to promote rapid crystallization. The capillary was sealed with hot wax. Once mounted onto the goniometer and aligned, the sample was quenched in a custom-built cryostream system (Cryo Industries of America Inc, Manchester, NH, USA) to 82 K. The nitrogen gas-flow was aligned co-axial with the capillary to avoid capillary icing in the absence of a shield-gas as shown in Supplementary Figure S1. A heat shield (Crystal Positioning Systems, Jamestown, NY, USA) was attached to the goniometer head to prevent icing. The co-axial nozzle geometry inevitably has a temperature gradient along the sample but is constant to approximately 10 mm from the cryostream nozzle tip (Whitfield et al., 2010).

Data were collected in Debye–Scherrer geometry on a Cu $K\alpha$ Bruker-AXS D8 powder diffractometer with a focusing primary mirror and a Vantec-1 position sensitive detector (PSD). The use of fixed slit knife-edges on both primary and secondary beam-paths allowed data to be collected down to $5^\circ 2\theta$ while maintaining a low background even with the full 10° detector window. The temperature of the gas stream was expected to be stable for about 10 mm from the end of the nozzle (Whitfield et al., 2010). An 8 mm wide Debye (equatorial) slit was used to stop-down the 16 mm wide window of the Vantec PSD detector, masking out regions of the capillary where the temperature uniformity was expected to degrade rapidly. No distinct reflections were observed above $90^\circ 2\theta$ so datasets were collected between 5° and $90^\circ 2\theta$ in continuous scan mode with a nominal step size of 0.0214° and a 0.1 s effective count time. A cooling experiment was performed from 243 to 98 K in 5 K steps to obtain crystalline lattice parameters across the temperature range. The instrument was calibrated with a 0.5 mm capillary of NIST SRM640c silicon, and the zero-point error was fixed during subsequent analyses. The temperature calibration of the cryostream was verified via thermal expansion of a high-purity aluminum powder sample in a 0.5 mm capillary and the low-temperature phase transitions of ammonium nitrate as described in Whitfield et al. (2010).

The data were analyzed using TOPAS version 6 (Coelho et al., 2011). Indexing was carried out using the least-squares iteration (LSI) algorithm (Coelho, 2003). Pawley refinements were carried out to determine background and peak profile parameters. Any residual 2θ offsets were corrected via geometric corrections for capillary displacements parallel and perpendicular to the primary X-ray beam.

Simulated annealing in TOPAS was carried out with a z-matrix description of the 3-HPN molecule using typical bond lengths (Allen et al., 1987) and idealized angles from the valence-shell electron-pair repulsion method (VSEPR) (DeKock and Gray, 1980). The possible rotation around the

single carbon–carbon bond was allowed within the z-matrix during simulated annealing to allow the molecule to change conformation (e.g. *gauche*, *trans*). To account for preferred orientation a spherical harmonics correction (Järvinen, 1993) was applied with the coefficients reset to zero at the beginning of each cycle to maintain stability (Whitfield, 2009).

The structures obtained were refined with the addition of a capillary absorption correction (Sabine et al., 1998) assuming a 100% dense sample. Isotropic atomic displacement parameters were refined for each element with the following restraints:

non-nitrile carbon $B_{\text{iso}} = \text{equal}$; hydrogen atoms = $1.8 \times B_{\text{iso}}$ of attached atom

Refined structures were optimized with fixed unit cell, dispersion-corrected density functional theory (DFT) calculations in Quantum Espresso v7.2 (Giannozzi et al., 2017). An initial optimization using BLYP generalized gradient approximation (GGA) pseudopotentials (Mardirossian and Head-Gordon, 2017) with a Becke–Johnson weighted DFT-D3 (Grimme et al., 2011) dispersion correction (DFT-D3(BJ)) was followed by a second optimization with the more computationally intensive B3LYP hybrid pseudopotential (Mardirossian and Head-Gordon, 2017) with the same dispersion correction. Force and energy convergence thresholds of 10^{-3} and 10^{-4} Rydberg atomic units (Ry) were used, respectively, with kinetic energy cutoffs for wavefunctions, charge densities, and exact exchange of 60, 240, and 240 Ry (equivalent to 816, 3265, and 3265 eV). Once the intramolecular structure (bond lengths, angles, torsions) was optimized, new z-matrices were constructed for a final refinement against the experimental data. The only aspect of the molecular geometry allowed to refine at this final stage was rotation around the sp^3 – sp^3 carbon to carbon bond. Full pdCIF files were generated and figures were created using the pdCIFplotter program (Rowles, 2022).

The IR data in Schneider and Giguère (1969) are presented in tabulated form only, but the corresponding doctoral thesis (Schneider, 1969) contained plots of the experimental IR and far-IR data collected at 93 K. The availability of the experimental data for both crystalline forms created the opportunity for a limited independent consistency-check of the two crystal structures. Quantum Espresso can calculate IR spectra from a crystalline structure via density functional perturbation theory (DFPT). Unfortunately, the high-level hybrid B3LYP functional and DFT-D3(BJ) dispersion correction used for the structure optimizations is not yet supported for phonon calculations in Quantum Espresso. Norm-conserving BLYP pseudopotentials (Mardirossian and Head-Gordon, 2017) and 2-body DFT-D3 (Grimme et al., 2010) dispersion corrections were used in their place after a benchmarking process to assess their suitability. Structures using lattice parameters obtained at 84 K were relaxed with significantly tighter thresholds given the extreme sensitivity of phonon calculations. Force and energy convergence thresholds of 10^{-5} and 10^{-6} Rydberg atomic units (Ry) were used, respectively, with kinetic energy cutoffs for wavefunctions and charge densities of 120 and 480 Ry (1632 and 6530 eV). Effects of particle morphology on the spectra were calculated using an effective medium method with the program PDIElec (Kendrick and Burnett, 2016). A Lorentzian broadening of 10 cm^{-1} and

Mie scattering with a particle size of $2.5 \mu\text{m}$ appeared to yield relative intensities broadly consistent with observations for a number of other crystalline molecular compounds and were applied when plotting the 3-HPN results.

III. RESULTS

The diffraction patterns obtained on multiple crystallizations were observed to lack consistency as seen in Supplementary Figure S2. The most likely explanation for these otherwise puzzling results is two different crystalline phases can form and co-exist, one probably being metastable. Many crystallizations produced what appeared to be single-phase patterns with a phase that could exist from 84 K to melting. Several patterns had numerous peaks visible from one or more second minority phases. A single dataset collected at 218 K appeared to be essentially a pure specimen of what appeared to be a single, metastable phase. A comparison of the seemingly more common pure-phase pattern with that from the proposed second phase can be seen in Figure 1. Ramp-soak data collection on heating did not reveal any solid–solid phase transitions and two-phase mixtures were found to be possible in the full range of temperatures accessible below melting down to the base temperature of 84 K achievable with the cryostream. A slow crystallization experiment obtained reflection positions consistent with the more common phase alone with no solid–solid phase transitions as seen in the surface plot of Supplementary Figure S3. The lattice parameters obtained from Pawley refinement of the corresponding crystalline datasets are plotted in Supplementary Figure S4. The volume contraction was close to linear in the region between 173 and 103 K, yielding a volumetric thermal expansion coefficient of $65.5 \times 10^{-6} \text{ K}^{-1}$ at 173 K. This value is quite low compared to the mean value of $161 \times 10^{-6} \text{ K}^{-1}$ found by a survey of organic molecular crystals (Bond, 2021). A diffraction pattern collected at 183 K was chosen to represent the more common phase as it had better counting statistics and a wider 2θ range than the other datasets.

Indexing of the 183 K dataset in Figure 1 readily found a solution using 25 peak positions between 9.7 and $46.6^\circ 2\theta$, with tolerances of 0.02° , max $N_{\text{calc}}/N_{\text{obs}}$ of 2, and no zero-

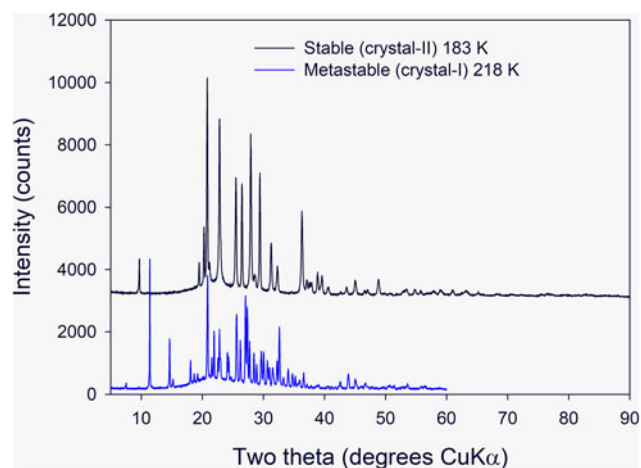


Figure 1. Raw data of the stable phase at 183 K and metastable phase at 218 K. The 183 K data have been displaced vertically by 3000 counts to improve clarity.

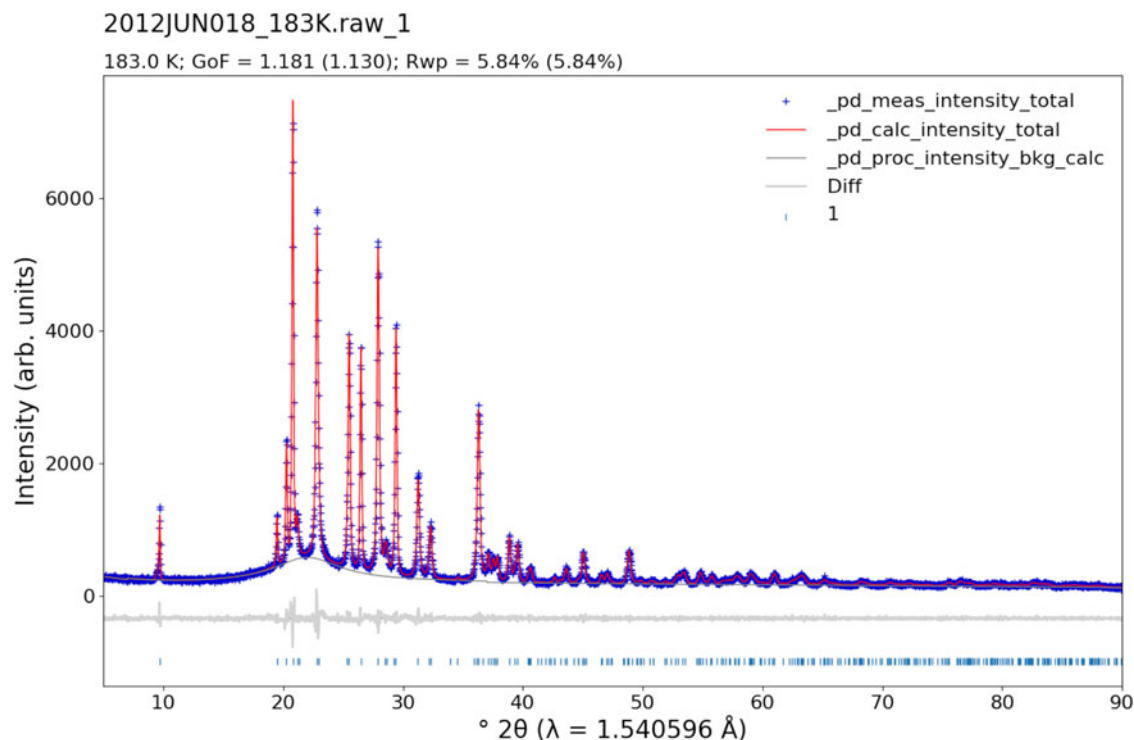


Figure 2. Pawley fit using the proposed orthorhombic unit cell with *Pbca* reflection conditions. $R_{wp} = 7.2\%$.

point error. The top solution with a goodness of fit (GoF) of 22.8 was an orthorhombic unit cell with the suggested extinction symbol of *Pbca*:

$$a = 18.203 \text{ \AA}, b = 4.998 \text{ \AA}, c = 8.530 \text{ \AA}, V = 774.6 \text{ \AA}^3$$

The *Pbca* extinction symbol has no alternate setting, so the proposed space group was also *Pbca*. A Pawley refinement of this unit cell against the 183 K dataset yielded the fit shown in Figure 2 with an R_{wp} residual of 5.84% and no obvious issues suggesting an incorrect unit cell or space group. A small amount of *hkl*-dependent peak broadening was modeled empirically using a fourth-order spherical harmonics Lorentzian peak broadening (R_{wp} value prior to application of the broadening model was 7.2%). The refined lattice parameters were:

$$a = 18.2118(8) \text{ \AA}, b = 4.9912(3) \text{ \AA}, c = 8.5358(5) \text{ \AA}, \\ V = 775.90(7) \text{ \AA}^3$$

These unit cell parameters were then used for the structure solution via simulated annealing. A satisfactory refinement was readily obtained. After structure optimization using the two-step DFT calculation the final Rietveld refinement versus the data produced the fit shown in Figure 3. The quality of fit ($R_{wp} = 6.54\%$; GoF = 1.28) is good for laboratory powder diffraction data. There are no concerning misfits from issues in either peak intensities or peak profiles. The cumulative χ^2 curve shows the expected features with main contributions from small misfits in the major reflections, and otherwise distributed across 2θ . The texture index of 1.06 derived from the preferred orientation correction is consistent with a noticeable but minor texture.

The structure of the crystal-II form is shown in Figure 4 with the details and atomic coordinates given in Table I. The molecules form O–H...O hydrogen bonds in a zig-zag (2_1 helical screw) running parallel to the *b*-direction. The direction of the hydrogen bonding alternates along the *c*-direction forming a pseudo-layered arrangement. The only intermolecular interactions involving the nitrile groups are weak hydrogen bonds with adjacent C–H. Hydrogen bonds involving C–H groups are weak and are less directional than conventional hydrogen bonds (Steiner, 2002). The impact of the empirical *hkl*-dependent peak broadening is highlighted in Supplementary Figure S5 where the correction was commented out, without running the least-squares minimization. The reflections whose full width at half maximum (FWHM) is not impacted by this are those where $l=0$. The structure in Figure 4 has a natural slip-plane in the *b*–*c* plane. Reflections that might be expected to be affected by slippage in this plane such as 600 and 410 are not. If the classical inverse relationship between cell dimensions and crystallite growth behavior is maintained, it is possible that the crystallite shape is responsible for the observed broadening.

The molecules of the *Pbca* $Z' = 1$ crystal-II structure are in the gauche conformation as seen in Figure 5. As mentioned earlier this is the most stable (Roux et al., 2007) with significant intramolecular interaction between the hydroxyl group and the π -electrons of the adjacent nitrile group. The nitrile group does not appear to participate in significant intermolecular interactions (Figure 4).

The indexing of the second, crystal-I form was less straightforward with noisier data, indistinct shoulders on many peaks, and the presence of some minor peaks from the other form. An indexing solution was found to a primitive monoclinic crystal system using 25 peak positions between 7.5 and 30° 2θ . A large number of solutions with a volume

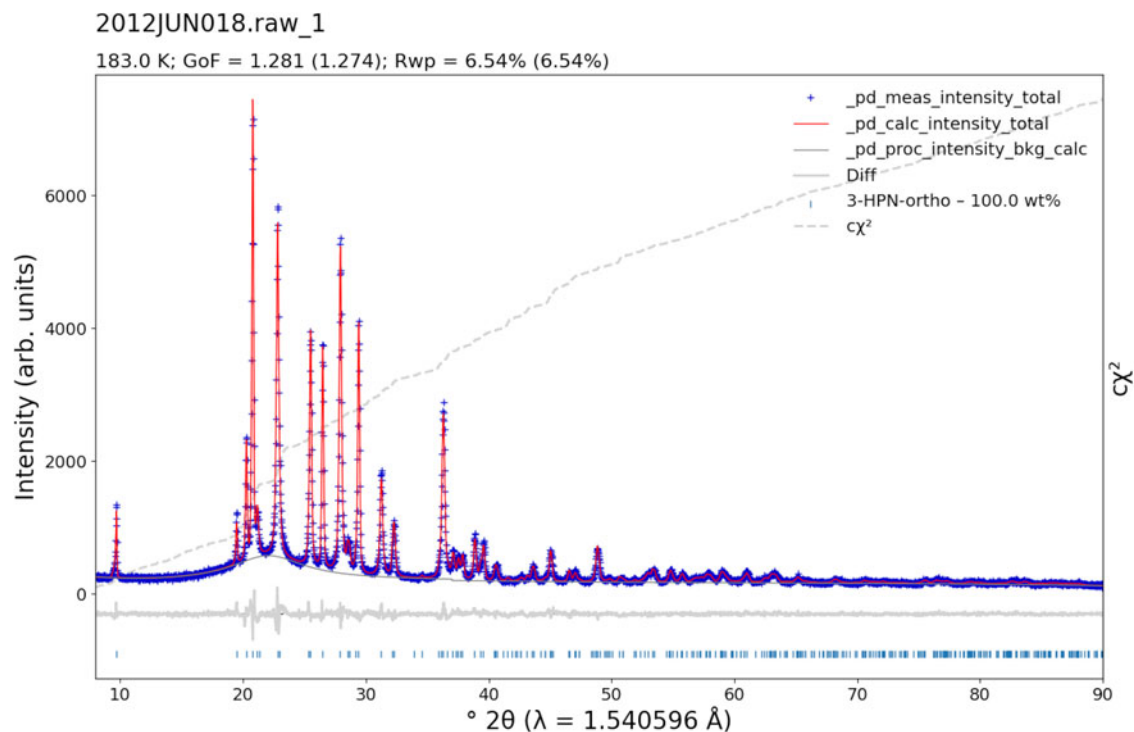


Figure 3. Rietveld difference plot for the refinement of the orthorhombic form from the DFT-optimized starting point versus one of the pure-phase patterns at 183 K.

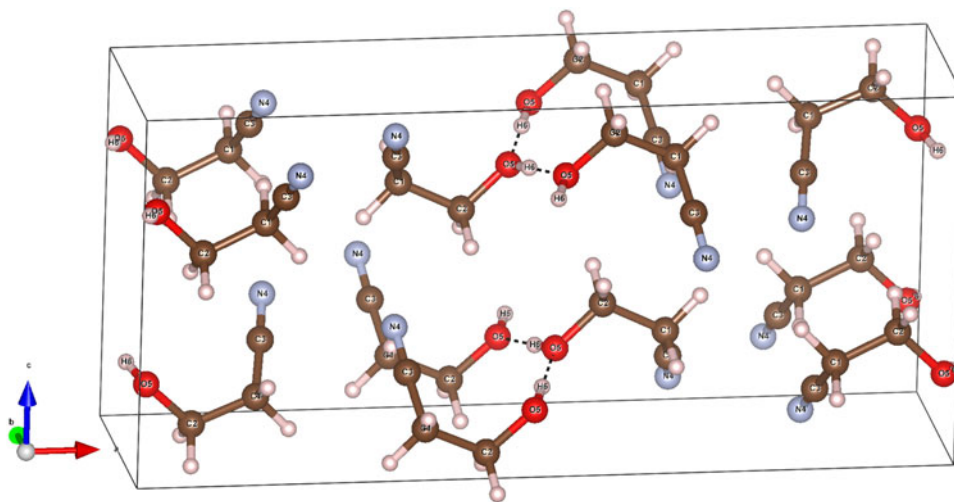


Figure 4. View of the final refined structure of the orthorhombic form showing the zig-zag chain of O-H...O hydrogen bonds running in the *b*-direction.

of 1198 \AA^3 were clustered as the top solutions. Solutions with equivalent cell dimensions with extinction symbols $P2$ and $P2_1$ had almost identical GoF values of 18. Using a large number of peaks from laboratory data to fairly high 2θ angles this GoF was highly promising. A series of Pawley fits to the data found that the space group $P2_1/n$ could model the data equally well, so as the higher symmetry solution, this was used for the simulated annealing stage. Unlike for crystal-II, no hkl -dependent peak broadening was noticeable in the crystal-I data. The refined unit cell parameters from the Pawley refinement were:

Space group: $P2_1/n$, $a = 23.475(1) \text{ \AA}$, $b = 6.0031(4) \text{ \AA}$,
 $c = 8.5260(8) \text{ \AA}$, $\beta = 95.509(3)^\circ$, $V = 1196.0(2) \text{ \AA}^3$

This combination of unit cell volume and space group is consistent with three independent molecules in the unit cell, i.e. $Z' = 3$ and $Z = 12$.

Following the same basic refinement-optimize-refinement workflow as used for the orthorhombic structure, a final refined structure with DFT-optimized molecules was obtained. One difference in the procedure was the need to manually relocate the hydroxyl hydrogen atom of one of the 3-HPN molecules to reestablish the hydrogen bond with the adjacent molecule prior to the DFT optimization. The final Rietveld refinement fit to the data is shown in Figure 7. The fit is reasonable for what was a rapidly collected, noisy dataset across limited 2θ , with R_{wp} of 8.83% and GoF of 1.75. There are some visible misfits in peak profiles that are responsible for

TABLE I. Atomic coordinates of the orthorhombic crystal-II phase of 3-HPN at 183 K

Atom label	<i>x</i>	<i>y</i>	<i>z</i>	<i>B</i> _{iso}
C(1)	0.84300(8)	0.6771(10)	0.8239(5)	2.23(14)
C(2)	0.91940(11)	0.6498(12)	0.8985(5)	2.23(14)
C(3)	0.82876(14)	0.4655(12)	0.7111(6)	3.6(3)
N(4)	0.8197(2)	0.2981(16)	0.6202(9)	3.56(19)
O(5)	0.97682(9)	0.6652(14)	0.7845(7)	3.61(14)
H(6)	0.99325(13)	0.4843(15)	0.7576(9)	6.5(3)
H(7)	0.80091(11)	0.6701(12)	0.9150(5)	4.0(3)
H(8)	0.83794(16)	0.8689(10)	0.7635(6)	4.0(3)
H(9)	0.9230(2)	0.4633(14)	0.9643(8)	4.0(3)
H(10)	0.92667(14)	0.8147(15)	0.9803(6)	4.0(3)

Space group: *Pbca*, *Z* = 8, *Z'* = 1
a = 18.218(2) Å, *b* = 4.9931(7) Å, *c* = 8.5387(11) Å, *V* = 776.7(2) Å³
 $\rho_x = 1.2157(3)$ g cm⁻³
Texture index = 1.051(2) (Bunge, 1982)
T = 183 K; *R*_{wp} = 6.5%.

All occupancies = 1.

the major jumps in the cumulative χ^2 curve. An overview of the resulting structure is shown in Figure 8. The *B*_{iso} isotropic displacement parameters for the atoms were constrained to be the same across the three independent molecules. The signal-to-noise of the dataset for the refinement of the *P2*₁/*n* structure was higher and was collected over a narrower 2θ range. Consequently, the *B*_{iso} was described using a scaling factor applied to the *B*_{iso} obtained with the better-quality *Pbca* dataset. This naturally applied a constraint such that each equivalent atom in the three molecules had the same *B*_{iso}. The final coordinates for the *P2*₁/*n* structure are given in Table II.

The crystal-I structure arranges the 3-HPN molecules to produce a pseudo-3₁ helical chain of O–H...O hydrogen bonds along the *b*-direction. Unusually high *Z'* values with

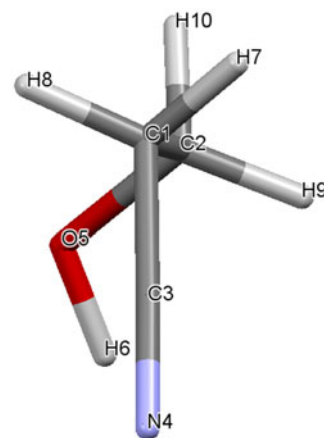


Figure 5. *Gauche* conformation of the 3-HPN molecule in the crystal-II phase showing how the hydroxyl and nitrile groups arrange themselves relative to each other.

helical hydrogen bonding have been observed previously in mono-alcohols with bulky secondary groups (Brock and Duncan, 1994). Two of the 3-HPN molecules are in the same energetically favored *gauche* conformation as the orthorhombic phase. The third molecule is in a less energetically favorable “anti-*gauche*” conformation (Roux et al., 2007) as seen in Figure 9. Here the hydrogen atom of the hydroxyl group breaks the intramolecular interaction with the nitrile π -electrons to create an intermolecular hydrogen bond with the oxygen atom of an adjacent HPN molecule.

The directions of the hydrogen bonding chains also differ from the crystal-II structure. Rather than clustering in layers in the *ab* plane, the H-bond directions alternate in blocks along the *a* direction with all the H-bond chains in half the unit cell running one way along *b*, and the opposite direction in

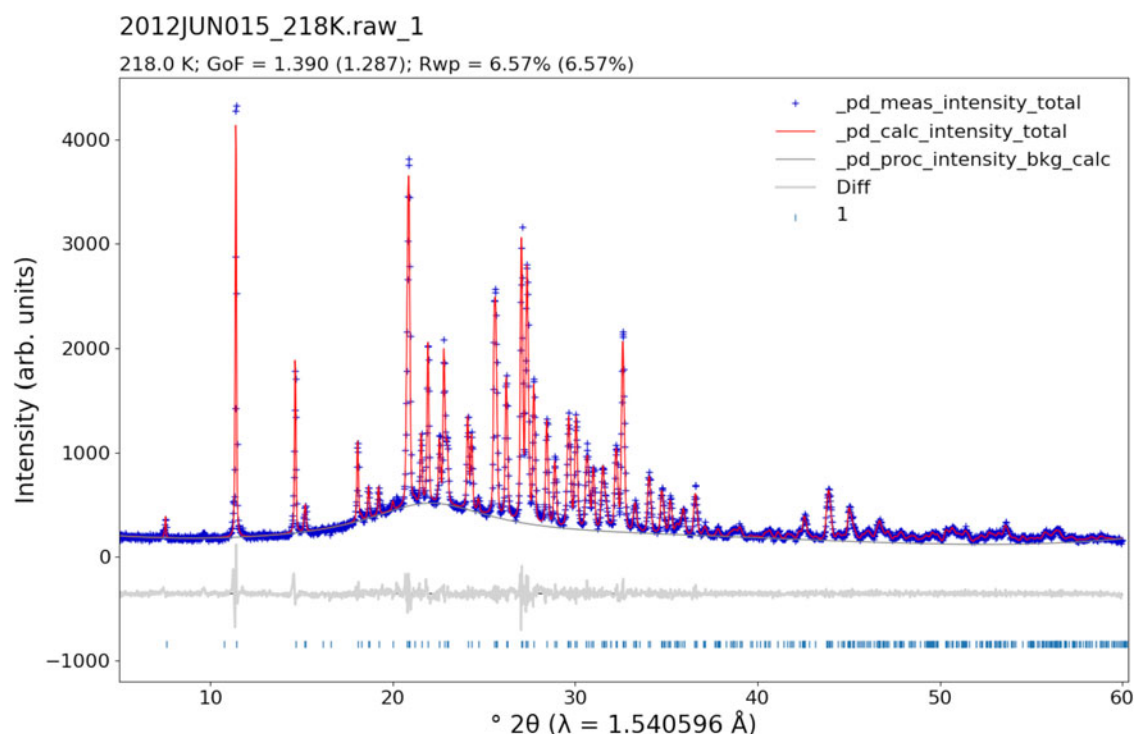


Figure 6. Pawley fit using a primitive monoclinic unit cell with *P2*₁/*n* reflection conditions. *R*_{wp} = 7.0%.

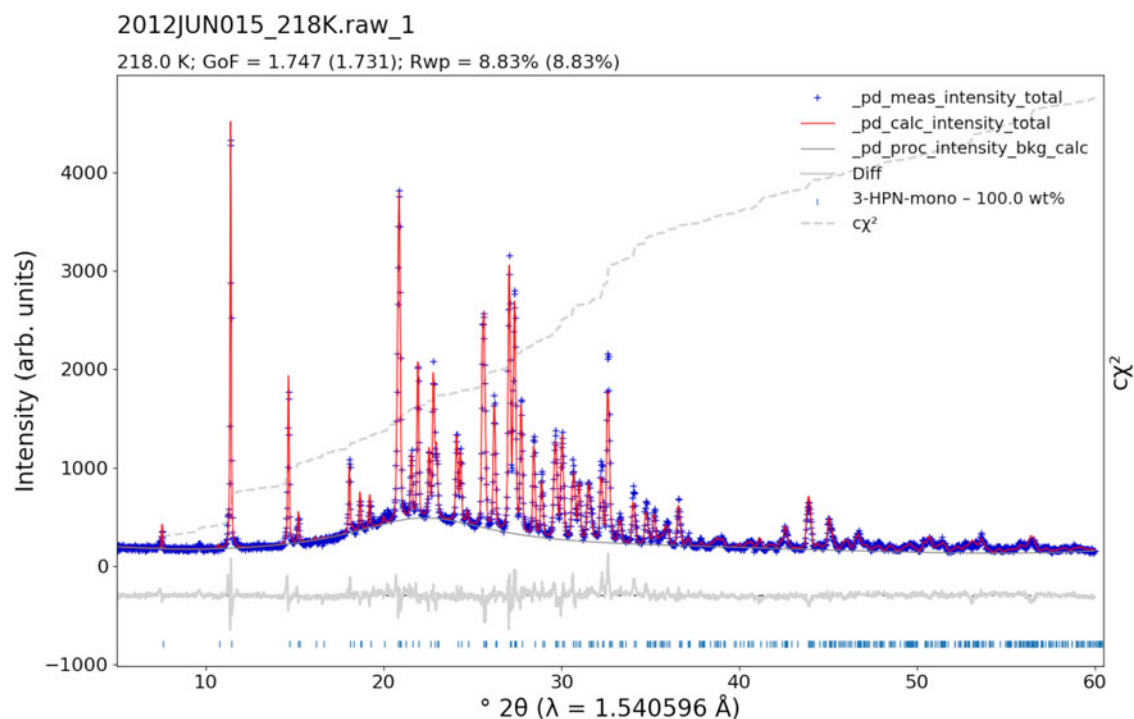


Figure 7. Rietveld difference plot for the refinement of the monoclinic form at 218 K.

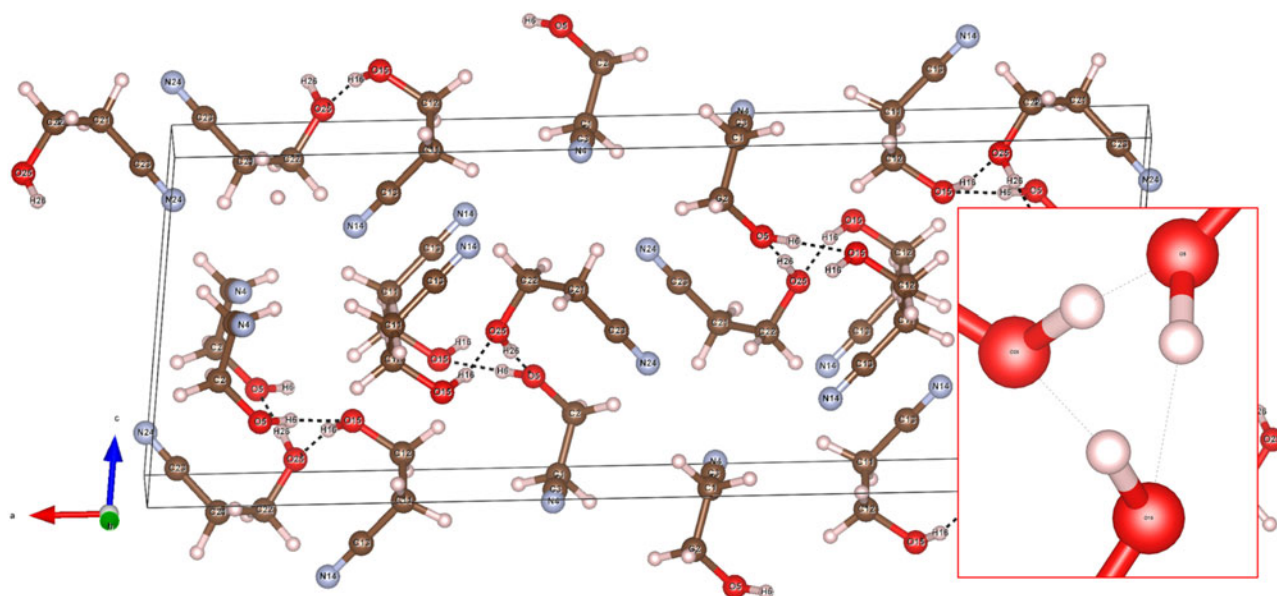


Figure 8. View of the final refined structure of the monoclinic form showing the helical chains of O–H...O hydrogen bonds running parallel to the *b*-direction. The insert shows the hydrogen bonding along *b*^{*}, highlighting the characteristic triangle of a 3₁-like screw axis.

the other half. A comparison of the O–H...O hydrogen bonding environment between the orthorhombic and monoclinic structures is given in Table III. The hydrogen bonding in the orthorhombic phase appears to be stronger with a near-linear bond and moderate donor-to-acceptor distance. Two of the three donor–acceptor distances in the hydrogen bonds of crystal-I are similar to those of the crystal-II structure, but the hydrogen bonding environment is more distorted overall. The hydroxyl group of the anti-*gauche* molecule in the

crystal-I structure has the shortest donor–acceptor distance of the three.

An overview of the weak intermolecular hydrogen bonds of the nitrogen atoms with adjacent carbon-bonded hydrogens for both structures is given in Table IV. Within a contact distance of 3 Å, all the nitrogen atoms can be considered as 4-coordinate. However, the van der Waals sum of nitrogen and hydrogen from the values in Bondi (Bondi, 1964) is 2.72 Å. Bondi stated that their tabulated radii may not be

TABLE II. Atomic coordinates of the monoclinic crystal-I phase of 3-HPN at 218 K

Atom label	<i>x</i>	<i>y</i>	<i>z</i>	<i>B</i> _{iso}
C(1)	0.0753(4)	0.2436(15)	0.5021(7)	1.74(18)
C(2)	0.0651(6)	0.3112(19)	0.6710(9)	1.74(18)
C(3)	0.0820(7)	0.0033(15)	0.4851(11)	1.79(18)
N(4)	0.0869(10)	-0.1871(16)	0.4723(16)	1.86(19)
O(5)	0.1126(8)	0.258(3)	0.7828(9)	2.0 (2)
H(6)	0.1429(8)	0.372(3)	0.7842(12)	3.7(4)
H(7)	0.0390(5)	0.2947(19)	0.4200(10)	3.1(3)
H(8)	0.1132(5)	0.327(2)	0.4644(10)	3.1(3)
H(9)	0.0282(7)	0.222(3)	0.7083(12)	3.1(3)
H(10)	0.0589(11)	0.494(3)	0.6708(17)	3.1(3)
C(11)	0.7621(4)	0.1910(19)	0.5234(9)	1.74(18)
C(12)	0.7593(7)	-0.007(2)	0.4080(10)	1.74(18)
C(13)	0.7239(4)	0.166(3)	0.6477(10)	1.79(18)
N(14)	0.6936(6)	0.145(4)	0.7458(13)	1.86(19)
O(15)	0.7051(8)	-0.022(3)	0.3153(13)	2.0 (2)
H(16)	0.6835(11)	-0.149(4)	0.3539(16)	3.7(4)
H(17)	0.8060(4)	0.208(3)	0.5778(10)	3.1(3)
H(18)	0.7515(6)	0.346(2)	0.4604(10)	3.1(3)
H(19)	0.7685(11)	-0.162(2)	0.4722(13)	3.1(3)
H(20)	0.7924(7)	0.020(3)	0.3284(11)	3.1(3)
C(21)	0.9236(3)	0.3157(16)	0.9241(11)	1.74(18)
C(22)	0.875(2)	0.143(8)	0.9120(19)	1.74(18)
C(23)	0.9697(9)	0.257(9)	1.0440(14)	1.79(18)
N(24)	1.0054(15)	0.209(15)	1.1409(19)	1.86(19)
O(25)	0.848(2)	0.126(12)	1.056(2)	2.0 (2)
H(26)	0.866(4)	0.003(9)	1.121(3)	3.7(4)
H(27)	0.9408(5)	0.330(3)	0.8098(12)	3.1(3)
H(28)	0.9074(19)	0.480(3)	0.9528(16)	3.1(3)
H(29)	0.891(4)	-0.019(6)	0.878(3)	3.1(3)
H(30)	0.8425(13)	0.200(14)	0.821(2)	3.1(3)

Space group: $P2_1/n$, $Z = 12$, $Z' = 3$

$a = 23.420(19)$ Å, $b = 5.989(5)$ Å, $c = 8.506(7)$ Å, $\beta = 95.508(3)^\circ$, $V = 1187.6(17)$ Å³

$\rho_x = 1.1926(17)$ g cm⁻³

Texture index = 1.131(5) (Bunge, 1982)

$T = 218$ K; $R_{wp} = 8.8\%$

All occupancies = 1.

suitable for the calculation of contact distances, but Table IV uses the resulting sum as a convenient cutoff to identify consequential N...H-C interactions. It is interesting to note that the anti-*gauche* molecule in the $P2_1/n$ structure appears to interact more strongly than any other, including that of the more commonly occurring orthorhombic structure. The

interactions will be significantly weaker than those involving the hydroxyl groups, so it is more likely a result of the distortion of the molecule to the anti-*gauche* conformation rather than a driving force for it.

The multi-phase datasets afforded the opportunity to obtain the structures and cell parameters for each of the phases under identical conditions. Comparing the energies for the different forms at 183 and 218 K, respectively, can give an indication of their relative stabilities, but the volume difference due to thermal expansion always adds a degree of uncertainty. Using data from refinement of a multi-phase refinement such as that seen in Figure 10 removes that source of uncertainty. There are no visible unindexed reflections in Figure 10 and the fit to the data is very good. DFT optimization for both phases using lattice parameters derived from the 84 K dataset shown in Table V yielded an energy difference < 0.5 kJ mol⁻¹ between the two structures, the crystal-II structure being only slightly more stable than the crystal-I structure. Such a small difference in energy is slightly surprising given the difference in cell volume per formula unit at 84 K; 95.8 versus 97.9 Å³ for the crystal-II and crystal-I structures, respectively, and the hydrogen bond environments in Table III. However, DFT calculations consider all aspects of the crystal structure such as the van der Waals interactions and steric interactions as well as the density of the structure.

Schneider (1969) collected vibrational spectroscopy data for the crystalline forms at 93 K. The refined 84 K lattice parameters for the two phases should be close enough to the unit cells at 93 K to improve the chances of calculating reasonable IR spectra via phonon calculations. Schneider (1969) identified the region in the far-IR between 40 and 350 cm⁻¹ as exhibiting the clearest differences between the two crystalline forms. Comparisons between the experimental and calculated transmission curves are shown in Figures 11(a) and 11(b) for monoclinic crystal-I and orthorhombic crystal-II, respectively. Given the limitations of phonon calculations in such molecular systems, the agreement between experimental and calculated data is quite good. In particular, the lack of any bands between 225 and 350 cm⁻¹ in the crystal-II experimental data provides a clear fingerprint for the presence of crystal-I in Figure 11(a).

Schneider and Giguère (1969) assigned the additional bands in crystal-I as equivalent to the *trans* conformation observed in the liquid phase as they did not consider other

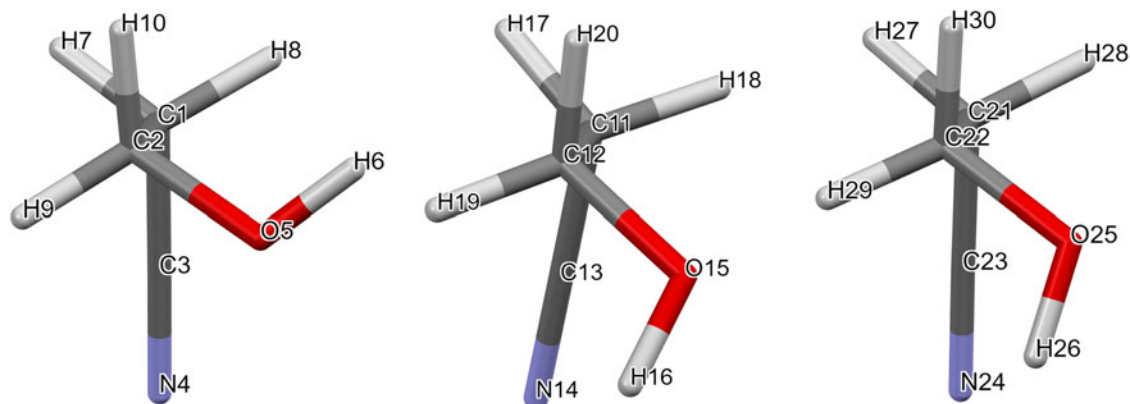


Figure 9. Conformations of the three independent 3-HPN molecules in the crystal-I phase.

TABLE III. Comparison of the O–H...O hydrogen bonding environments in the orthorhombic and monoclinic phases from the final refined structures

Phase	H-bond	D–A distance (Å)	D–H...A angle (°)
Crystal-II	O(5)–H(6)...O(5)	2.701(9)	178.4(7)
Crystal-I	^a O(5)–H(6)...O(15)	2.68(3)	166(2)
	O(15)–H(16)...O(25)	2.73(6)	172(2)
	O(25)–H(26)...O(5)	2.79(6)	168(8)
	Mean	2.73	169

^aAnti-*gauche*.

modifications. The use of a DFPT calculation gives an advantage over the experimental paper in that the modes responsible for each absorption band are automatically obtained. Consequently, the modes responsible for the bands at 300 and 305 cm⁻¹ in crystal-I can be identified to determine if they correlate with the OH...O hydrogen bonding chain.

The signature crystal-I mode close to 300 cm⁻¹ is closely related to the hydrogen bonding chain. The motion involves a twisting of the molecule around the central C–C bond with the

TABLE IV. Comparison of the weak C–H...N intermolecular hydrogen bonding environments in the crystal-II and crystal-I phases from the final refined structures

Phase	Conformation	H-bond	H...N distance (Å)	C–H...N angle (°)
Crystal-II	<i>Gauche</i>	C(1)–H(8)...N(4)	2.490(10)	176.8(4)
		C(2)–H(9)...N(4)	2.649(9)	129.6(4)
		C(1)–H(7)...N(4)	2.815(7)	171.5(5)
		C(2)–H(10)...N(4)	2.994(9)	131.7(3)
		Mean	2.737	152.4
Crystal-I	<i>Anti-gauche</i>	C(21)–H(27)...N(4)	2.571(18)	136.4(12)
		C(11)–H(17)...N(4)	2.59(3)	144.6(9)
		C(2)–H(10)...N(4)	2.710(19)	129.8(12)
		C(2)–H(9)...N(4)	2.98(3)	126.0(10)
		Mean	2.713	134.2
	<i>Gauche</i>	C(12)–H(19)...N(14)	2.733(19)	146.4(12)
		C(1)–H(8)...N(14)	2.775(18)	147.8(10)
		C(22)–H(30)...N(14)	2.84(9)	128(6)
		C(21)–H(28)...N(14)	2.94(4)	116.9(18)
		Mean	2.822	134.8
	<i>Gauche</i>	C(1)–H(7)...N(24)	2.48(3)	135.3(17)
		C(22)–H(29)...N(24)	2.70(10)	137(7)
		C(2)–H(10)...N(24)	2.89(7)	135.9(18)
		C(21)–H(28)...N(24)	2.93(8)	104(3)
		Mean	2.75	128.1

Only contacts within 3 Å are shown and distances within error of the N–H 2.72 Å van der Waals radii sum (Bondi, 1964) are in bold.

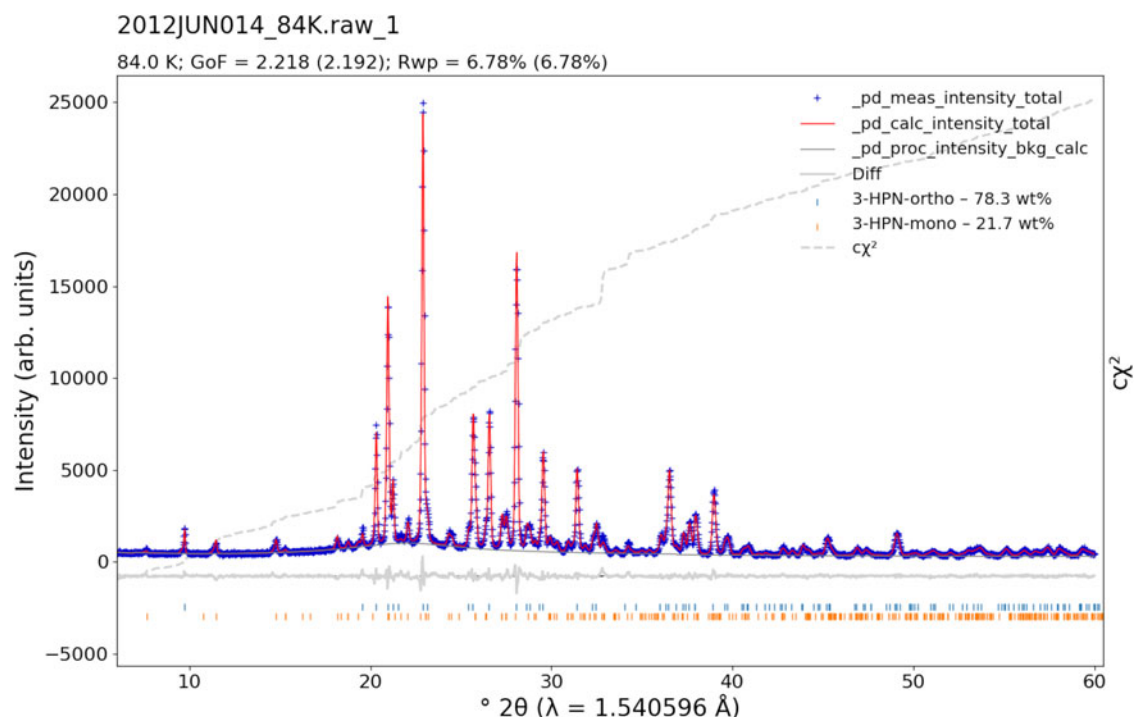


Figure 10. Two-phase refinement of a dataset collected at 84 K.

TABLE V. Lattice parameters obtained from Pawley refinement of the two-phase dataset in Figure 10 at 84 K

Phase	a (Å)	b (Å)	c (Å)	β (°)	V (Å ³)
Crystal-II	18.1430(15)	4.9850(4)	8.4751(7)	90	766.5(1)
Crystal-I	23.238(3)	5.978(1)	8.495(1)	95.414(9)	1174.7(3)

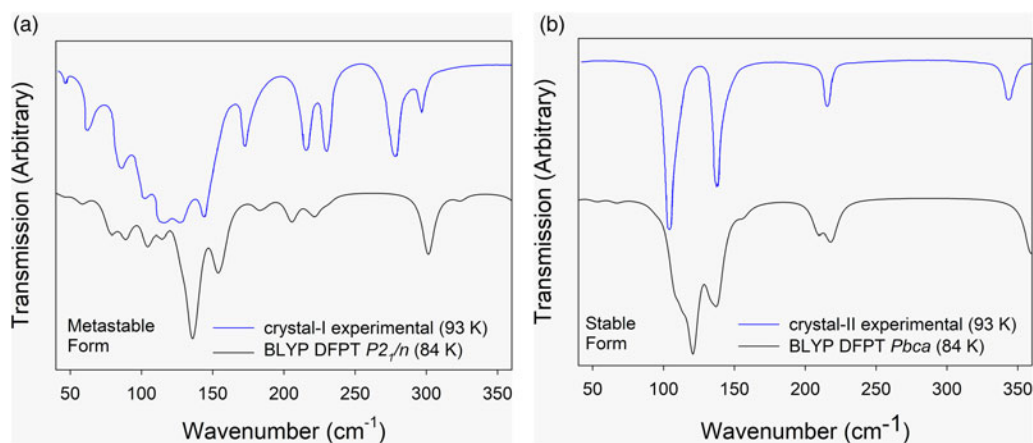


Figure 11. Comparison of experimental and DFPT-calculated far-IR region for (a) crystal-I and (b) crystal-II. Experimental data extracted from Schneider (1969).

hydroxyl end of the molecule wagging back and forth in a manner *anti* to the adjacent hydroxyl group. Such a motion would not readily be consistent with the symmetry of the crystal-II structure but is easily accessible to a structure with three independent molecules such as the crystal-I structure. Animations of the 300 cm⁻¹ crystal-I mode and associated crystal-II mode at 360 cm⁻¹ identified by the calculation are available as Supplementary material.

IV. CONCLUSION

Two different crystalline forms of 3-HPN were found to exist on *in situ* crystallization at low temperatures, one stable (crystal-II) and one seemingly metastable (crystal-I). The crystal structures of both have been solved via simulated annealing followed by DFT optimization and final refinement. The more stable crystal-II phase is orthorhombic in *Pbca* ($Z' = 1$) with the 3-HPN molecule in the energetically stable *gauche* conformation. A zig-zag chain of hydrogen bonding between the hydroxyl groups occurs along the *b*-direction. The metastable crystal-I phase is monoclinic *P2₁/n* ($Z' = 3$) with two molecules in *gauche* and one in *anti-gauche* conformation. A pseudo-3₁ helical hydrogen bonding chain is aligned with the unit cell *b*-direction. DFT computation using lattice parameters of both phases derived from a single 84 K dataset showed the difference in energy between the two structures to be less than 0.5 kJ mol⁻¹. This helps explain the observed phase behavior with wildly varying relative phase fractions on repeated crystallizations, albeit usually favoring the orthorhombic phase. The lack of any solid–solid transition remarked by Schneider (1969) explains the observed stability of the mixtures once formed. Far-IR data calculated from the refined 84 K unit cells of each phase are consistent with the literature 93 K experimental data. Consistency with complementary experimental data provides good supporting evidence for the veracity of the two structural models.

V. DEPOSITED DATA

“3-HPN_crystal_I.cif” Full pdCIF file containing raw diffraction data and Rietveld fit in addition to structure information for Crystal-I at 218 K.

“3-HPN_crystal_II.cif” Full pdCIF file containing raw diffraction data and Rietveld fit in addition to structure information for Crystal-II at 183 K.

“3-HPN_84K_2phase.cif” Full pdCIF file containing raw diffraction data and Rietveld fit for the two-phase refinement at 84 K.

The powder diffraction Crystallographic Information Framework (pdCIF) files were deposited with the ICDD. The data can be requested at pdj@icdd.com

Crystal structure CIF files deposited with CCDC (CCDC 2313841-2313842).

SUPPLEMENTARY MATERIAL

The supplementary material for this article can be found at <https://doi.org/10.1017/S0885715624000010>.

ACKNOWLEDGEMENTS

The authors would like to thank Professor Scott Mixture of Alfred University, New York, USA for reviewing the manuscript.

CONFLICTS OF INTEREST

The authors declare no conflicts of interest.

REFERENCES

- Abrahams, S. C., R. L. Collin, W. N. Lipscomb, and T. B. Reed. 1950. “Further Techniques in Single-Crystal X-Ray Diffraction Studies at Low Temperatures.” *Review of Scientific Instruments* 21 (4): 396–97. doi:10.1063/1.1745593.

- Abu-Lebdeh, Y., and I. Davidson. 2009. "High-Voltage Electrolytes Based on Adiponitrile for Li-Ion Batteries." *Journal of the Electrochemical Society* 156 (1): A60. doi:10.1149/1.3023084.
- Allen, F. H., O. Kennard, D. G. Watson, L. Brammer, A. Guy Orpen, and R. Taylor. 1987. "Tables of Bond Lengths Determined by X-Ray and Neutron Diffraction. Part 1. Bond Lengths in Organic Compounds." *Journal of the Chemical Society, Perkin Transactions 2* (12): S1. doi:10.1039/p298700000s1.
- Bond, A. D. 2021. "A Survey of Thermal Expansion Coefficients for Organic Molecular Crystals in the Cambridge Structural Database." *Acta Crystallographica Section B Structural Science, Crystal Engineering and Materials* 77 (3): 357–64. doi:10.1107/S2052520621003309.
- Bondi, A. 1964. "Van Der Waals Volumes and Radii." *The Journal of Physical Chemistry* 68 (3): 441–51. doi:10.1021/j100785a001.
- Braakman, R., A. Belloche, G. A. Blake, and K. M. Menten. 2010. "Search for Interstellar Methoxyacetonitrile and Cyanoethanol: Insights into Coupling of Cyano- to Methanol and Ammonia Chemistry." *The Astrophysical Journal* 724 (2): 994–1005. doi:10.1088/0004-637X/724/2/994.
- Brock, C. P., and L. L. Duncan. 1994. "Anomalous Space-Group Frequencies for Monoalcohols C_nH_mOH." *Chemistry of Materials* 6 (8): 1307–12. doi:10.1021/cm00044a030.
- Brodalla, D., D. Mootz, R. Boese, and W. Osswald. 1985. "Programmed Crystal Growth on a Diffractometer with Focused Heat Radiation." *Journal of Applied Crystallography* 18 (5): 316–19. doi:10.1107/S002188988501038X.
- Buckley, P., and P. A. Giguère. 1967. "Infrared Studies on Rotational Isomerism. I. Ethylene Glycol." *Canadian Journal of Chemistry* 45 (4): 397–407. doi:10.1139/v67-070.
- Buckley, P., P. A. Giguère, and M. Schneider. 1969. "Infrared Studies on Rotational Isomerism. III. 2-Chloro- and 2-Bromo-Ethanol." *Canadian Journal of Chemistry* 47 (6): 901–10. doi:10.1139/v69-148.
- Bunge, H.-J. 1982. *Texture Analysis in Materials Science: Mathematical Methods*. English ed. London; Boston: Butterworths.
- Coelho, A. A. 2003. "Indexing of Powder Diffraction Patterns by Iterative Use of Singular Value Decomposition." *Journal of Applied Crystallography* 36 (1): 86–95. doi:10.1107/S0021889802019878.
- Coelho, A. A., J. Evans, I. Evans, A. Kern, and S. Parsons. 2011. "The TOPAS Symbolic Computation System." *Powder Diffraction* 26 (S1): S22–25. doi:10.1154/1.3661087.
- David, W. I. F., and R. M. Ibberson. 1992. "A Reinvestigation of the Structure of Tetrahydrofuran by High-Resolution Neutron Powder Diffraction." *Acta Crystallographica Section C Crystal Structure Communications* 48 (2): 301–3. doi:10.1107/S0108270191008582.
- DeKock, R. L., and H. B. Gray. 1980. *Chemical Structure and Bonding*. Menlo Park, CA: Addison Wesley Longman, Benjamin-Cummings Publishing Company.
- Giannozzi, P., O. Andreussi, T. Brumme, O. Bunau, M. Buongiorno Nardelli, M. Calandra, R. Car, et al. 2017. "Advanced Capabilities for Materials Modelling with Quantum ESPRESSO." *Journal of Physics: Condensed Matter* 29 (46): 465901. doi:10.1088/1361-648X/aa8f79.
- Grauer, O. H., and E. H. Hamilton. 1950. "An Improved Apparatus for the Determination of Liquidus Temperatures and Rates of Crystal Growth in Glasses." *Journal of Research of the National Bureau of Standards* 44 (5): 495. doi:10.6028/jres.044.044.
- Grimme, S., J. Antony, S. Ehrlich, and H. Krieg. 2010. "A Consistent and Accurate *Ab Initio* Parametrization of Density Functional Dispersion Correction (DFT-D) for the 94 Elements H-Pu." *The Journal of Chemical Physics* 132 (15): 154104. doi:10.1063/1.3382344.
- Grimme, S., S. Ehrlich, and L. Goerigk. 2011. "Effect of the Damping Function in Dispersion Corrected Density Functional Theory." *Journal of Computational Chemistry* 32 (7): 1456–65. doi:10.1002/jcc.21759.
- Ibberson, R. M., W. I. F. David, O. Yamamuro, Y. Miyoshi, T. Matsuo, and H. Suga. 1995. "Calorimetric, Dielectric, and Neutron Diffraction Studies on Phase Transitions in Ordinary and Deuterated Acetone Crystals." *The Journal of Physical Chemistry* 99 (38): 14167–73. doi:10.1021/j100038a059.
- Järvinen, M. 1993. "Application of Symmetrized Harmonics Expansion to Correction of the Preferred Orientation Effect." *Journal of Applied Crystallography* 26 (4): 525–31. doi:10.1107/S0021889893001219.
- Kendrick, J., and A. D. Burnett. 2016. "PDIELEC: The Calculation of Infrared and Terahertz Absorption for Powdered Crystals." *Journal of Computational Chemistry* 37 (16): 1491–1504. doi:10.1002/jcc.24344.
- Krueger, P. J., and H. D. Mettee. 1965. "Spectroscopic Studies of Alcohols: V. Intramolecular Hydrogen Bonds in 2-Cyanoethanol and in Some Nitroalcohols." *Canadian Journal of Chemistry* 43 (10): 2888–95. doi:10.1139/v65-398.
- Mardirossian, N., and M. Head-Gordon. 2017. "Thirty Years of Density Functional Theory in Computational Chemistry: An Overview and Extensive Assessment of 200 Density Functionals." *Molecular Physics* 115 (19): 2315–72. doi:10.1080/00268976.2017.1333644.
- Misra, P. K., S. A. N. Hashmi, W. Haq, and S. B. Katti. 1989. "3-Hydroxypropionitrile: a New Reagent for Carboxyl Protection in Peptide Synthesis." *Tetrahedron Letters* 30 (27): 3569–72. doi:10.1016/S0040-4039(00)99443-7.
- Roux, M. V., R. Notario, E. Vélez, M. Temprado, A. Guerrero, S. P. Verevkin, J. Quijano, and J. Gaviria. 2007. "Experimental and Computational Thermochemical Study of 3-Hydroxypropanenitrile." *The Journal of Chemical Thermodynamics* 39 (10): 1377–83. doi:10.1016/j.jct.2007.03.011.
- Rowles, M. R. 2022. "pdCIFplotter: Visualizing Powder Diffraction Data in pdCIF Format." *Journal of Applied Crystallography* 55 (3): 631–37. doi:10.1107/S1600576722003478.
- Sabine, T. M., B. A. Hunter, W. R. Sabine, and C. J. Ball. 1998. "Analytical Expressions for the Transmission Factor and Peak Shift in Absorbing Cylindrical Specimens." *Journal of Applied Crystallography* 31 (1): 47–51. doi:10.1107/S0021889897006961.
- Schleyer, P. Von R., D. S. Trifan, and R. Bacskai. 1958. "Intramolecular Hydrogen Bonding Involving Double Bonds, Triple Bonds and Cyclopropane Rings as Proton Acceptors." *Journal of the American Chemical Society* 80 (24): 6691–92. doi:10.1021/ja01557a064.
- Schneider, M. 1969. Étude Spectroscopique de L'Isomérisation de Rotation dans les Éthanol 2-Substitués. DSc diss. Université Laval.
- Schneider, M., and P. A. Giguère. 1969. "Infrared Studies on Rotational Isomerism. IV. 2-Cyanoethanol." *Canadian Journal of Chemistry* 47 (24): 4685–90. doi:10.1139/v69-773.
- Steiner, T. 2002. "The Hydrogen Bond in the Solid State." *Angewandte Chemie International Edition* 41 (1): 48–76. doi:10.1002/1521-3773(20020104)41:1<48::AID-ANIE48>3.0.CO;2-U.
- Wang, H., H. Li, B. Xue, Z. Wang, Q. Meng and L. Chen 2005. "Solid-State Composite Electrolyte LiI/3-Hydroxypropionitrile/SiO₂ for Dye-Sensitized Solar Cells." *Journal of the American Chemical Society* 127(17), 6394–6401. doi:10.1021/ja043268p
- Wang, H., Z. Wang, B. Xue, Q. Meng, X. Huang, and L. Chen. 2004. "Polymer-in-Salt like Conduction Behavior of Small-Molecule Electrolytes." *Chemical Communications* (19): 2186. doi:10.1039/b406493c.
- Wang, H. X., Z. X. Wang, H. Li, Q. B. Meng, and L. Q. Chen. 2007. "Ion Transport in Small-Molecule Electrolytes Based on LiI/3-Hydroxypropionitrile with High Salt Contents." *Electrochimica Acta* 52 (5): 2039–44. doi:10.1016/j.electacta.2006.08.013.
- Whitfield, P. S. 2009. "Spherical Harmonics Preferential Orientation Corrections and Structure Solution from Powder Diffraction Data – A Possible Avenue of Last Resort." *Journal of Applied Crystallography* 42 (1): 134–36. doi:10.1107/S0021889808041149.
- Whitfield, P. S. 2023. "Low-Temperature Crystal Structures of the Solvent Dimethyl Carbonate." *Powder Diffraction* 38 (2): 100–111. doi:10.1017/S088571562300009X.
- Whitfield, P. S., Y. Le Page, A. Abouimrane, and I. J. Davidson. 2008. "Ab Initio Structure Determination of the Low-Temperature Phase of Succinonitrile from Laboratory X-Ray Powder Diffraction Data—Coping with Potential Poor Powder Quality Using DFT *Ab Initio* Methods." *Powder Diffraction* 23 (4): 292–99. doi:10.1154/1.3009635.
- Whitfield, P. S., A. Abouimrane, and I. J. Davidson. 2010. "In-Situ XRD Study of the Succinonitrile–Lithium Bis(Trifluoromethylsulfonyl)Imide (LiTFSI) Phase Diagram." *Solid State Ionics* 181 (15–16): 740–44. doi:10.1016/j.ssi.2010.04.004.